Numerical investigation of h-Darrieus wind turbine aerodynamics at different tip speed ratios

Kartik Venkatraman

Department of Mechanical Engineering, Université de Sherbrooke, Sherbrooke, Canada and Environment and Applied Fluid Dynamics, von Karman Institute for Fluid Dynamics, Sint-Genesius-Rode, Belgium

Stéphane Moreau

Department of Mechanical Engineering, Université de Sherbrooke, Sherbrooke, Canada, and

Julien Christophe and Christophe Schram

Environment and Applied Fluid Dynamics, von Karman Institute for Fluid Dynamics, Sint-Genesius-Rode, Belgium

Abstract

Purpose – The purpose of the paper is to predict the aerodynamic performance of a complete scale model H-Darrieus vertical axis wind turbine (VAWT) with end plates at different operating conditions. This paper aims at understanding the flow physics around a model VAWT for three different tip speed ratios corresponding to three different flow regimes.

Design/methodology/approach – This study achieves a first three-dimensional hybrid lattice Boltzmann method/very large eddy simulation (LBM-VLES) model for a complete scaled model VAWT with end plates and mast using the solver PowerFLOW. The power curve predicted from the numerical simulations is compared with the experimental data collected at Erlangen University. This study highlights the complexity of the turbulent flow features that are seen at three different operational regimes of the turbine using instantaneous flow structures, mean velocity, pressure iso-contours, blade loading and skin friction plots.

Findings – The power curve predicted using the LBM-VLES approach and setup provides a good overall match with the experimental power curve, with the peak and drop after the operational point being captured. Variable turbulent flow structures are seen over the azimuthal revolution that depends on the tip speed ratio (TSR). Significant dynamic stall structures are seen in the upwind phase and at the end of the downwind

phase of rotation in the deep stall regime. Strong blade wake interactions and turbulent flow structures are seen inside the rotor at higher TSRs.

Research limitations/implications – The computational cost and time for such high-fidelity simulations using the LBM-VLES remains expensive. Each simulation requires around a week using supercomputing facilities. Further studies need to be performed to improve analytical VAWT models using inputs/calibration from high fidelity simulation databases. As a future work, the impact of turbulent and nonuniform inflow conditions that are more representative of a typical urban environment also needs to be investigated.

Practical implications – The LBM methodology is shown to be a reliable approach for VAWT power prediction. Dynamic stall and blade wake interactions reduce the aerodynamic performance of a VAWT. An ideal operation close to the peak of the power curve should be favored based on the local wind resource, as this point exhibits a smoother variation of forces improving operational performance. The 3D flow features also exhibit a significant wake asymmetry that could impact the optimal layout of VAWT clusters to increase their power density. The present work also highlights the importance of 3D simulations of the complete model including the support structures such as end plates and mast.

Social implications – Accurate predictions of power performance for Darrieus VAWTs could help in better siting of wind turbines thus improving return of investment and reducing levelized cost of energy. It could promote the development of onsite electricity generation, especially for industrial sites/urban areas and renew interest for VAWT wind farms.

Originality/value – A first high-fidelity simulation of a complete VAWT with end plates and supporting structures has been performed using the LBM approach and compared with experimental data. The 3D flow physics has been analyzed at different operating regimes of the turbine. These physical insights and prediction capabilities of this approach could be useful for commercial VAWT manufacturers.

Keywords Vertical axis wind turbine, Tip speed ratio, Dynamic stall, Power curve, Blade wake interaction

Paper type Research paper

Abbreviations

TSR = tip speed ratio; and
VAWT = vertical axis wind turbine.

1. Introduction

Smart and sustainable city programs across the world have renewed the interest in decentralized electricity generation and sustainable building design. Small wind turbines in urban environments, more specifically Darrieus vertical axis wind turbines (VAWT) are well suited for urban areas. They operate independently of incoming wind direction without the need for an additional yawing mechanism. Moreover, studies have shown that they perform better in highly turbulent wind conditions encountered in a typical urban environment (Hannes, 2003).

Accurate aerodynamic and aeroacoustic performance prediction tools and well-informed siting are essential for the economic viability of these turbines. However, such predictions remain difficult due to the complex unsteady flow physics of Darrieus VAWTs, which comprise of dynamic stall and blade wake interactions. Several engineering models exist for the prediction of a VAWT power curve, such as the double multiple stream tube model based on the actuator disk modeling approach implemented in Q-Blade (Marten *et al.*, 2013). However, the computation of the blade forces is highly dependent on the input lift and drag polars of the blades to compute the forces and do not account for several flow phenomena such as the dynamic stall and tip vortices, which leads to significant inaccuracies and their applicability is restricted to large rotors with low solidity (ratio of the blade area to the rotor swept area) (Marten *et al.*, 2013).

Computational fluid dynamics (CFD) is more commonly used to study aerodynamics of VAWTs and most of the numerical studies have been performed using a two-dimensional

(2D) unsteady Reynolds-averaged Navier–Stokes (uRANS) approach (Amet *et al.*, 2009; Balduzzi *et al.*, 2016; Balduzzi *et al.*, 2020; Bianchini *et al.*, 2016; Biswas and Gupta, 2014; Rezaeiha *et al.*, 2017; Venkatraman *et al.*, 2021; Wu *et al.*, 2020).

However, several three-dimensional (3D) studies exist as well (Ardaneh *et al.*, 2021; Elkhoury *et al.*, 2015; Franchina *et al.*, 2019; Karimian and Abdolahifar, 2020; Lam and Peng, 2016; Posa, 2020b; Qin *et al.*, 2008; Zamre and Lutz, 2022). For instance, Qin *et al.* (2008) performed both 2D and 3D uRANS simulations of a simplified VAWT using a sliding mesh technique and found strong 3D effects such as the impact of tip vortices, including the interaction of supporting structure and losses at the blade tip, which resulted in power loss. Karimian and Abdolahifar (2020) performed 3D uRANS simulations of a three-part (3-PB) Darrieus turbine with straight blades and compared it to a helical Darrieus turbine, showing that 3-PB turbine performed produces a higher average torque with a smoother output. Ardaneh *et al.* (2021) then showed that the performance of the 3-PB turbine could be improved by setting an initial pitch angle to the blades to enhance the performance in the upwind phase of rotation by delaying dynamic stall. Yet, Franchina *et al.* (2019) that also studied the 3D flow physics of a two-bladed VAWT using a uRANS approach showed that the power prediction is highly dependent on the turbulence model and the numerical schemes being used. In fact, such a numerical approach cannot account for the actual 3D and turbulent/multiscale flows in such machines (Posa, 2020a), and therefore prevents any reliable comparison with actual experiments and particularly aeroacoustic experiments in open-jet anechoic wind tunnels. Li *et al.* (2013) achieved one of the first incompressible large eddy simulations (LES) on a limited span (what they called 2.5D) of a 3-NACA0015 blade H-Darrieus VAWT including the mast, at one single operating condition close to maximum efficiency. When compared to uRANS it improved performance predictions confirming results in Franchina *et al.* (2019), and showed more turbulent structures shed by the blades at an operating condition close to maximum efficiency. However, the short span simulation may have triggered too coherent turbulent structures and both grid and numerical schemes too dissipative to yield any significant interaction between the blades and the mast. Elkhoury *et al.* (2015) then performed the first 3D incompressible LES on a full three-blade H-Darrieus VAWT including mast and simplified connecting rods and was able to accurately predict the VAWT performance with both a fixed and a variable pitch mechanism. Yet, only large coherent structures near the blades were captured in these simulations and no significant interaction with the mast could be evidenced because of too much numerical dissipation. More recently, Posa and Balaras (2018) carried out a more resolved 3D LES of a simplified 3-NACA0022 blade H-Darrieus VAWT without supporting structures and mast to study the size and the impact of the turbulent coherent structures generated by the dynamic stall. Large coherent rollers are seen in the spanwise direction. These structures are produced during the upwind phase of the rotation due to the flow separation from the leading and trailing edges. Posa (2020b) also investigated the impact of spanwise flow features on the near wake of the turbine, showing an asymmetric wake feature produced by the turbine. Zamre and Lutz (2022) also achieved a scale-resolving 3D delayed detached eddy simulation to compute the flow around a roof-mounted VAWT under turbulent inflow conditions, showing that a skewed inflow has a positive impact on power performance at the operating tip speed ratio.

Yet, very little or no validation with experimental data and no consistent and systematic study has been performed with a high-fidelity turbulent simulation on a complete scale model VAWT with end plates and mast at different operating conditions. Indeed, the strong 3D flow features experienced by VAWTs highlight the necessity for high-fidelity 3D numerical simulations to account for the formation of tip vortices and interaction with the wind turbine mast and end plates. This motivates the present study to investigate the flow physics of a scaled model H-Darrieus VAWT with high solidity over different rotational speeds and power curve prediction under

uniform experimental inflow conditions using the low-dissipation, low-dispersion hybrid lattice Boltzmann method-very large eddy simulation (LBM-VLES). The Reynolds numbers (ranging from 25,000 to 500,000 based on chord length and wind speed) encountered in small urban Darrieus VAWTs make it necessary to use a turbulence model close to the wall. It is not feasible to resolve all relevant scales of motion using a direct numerical simulation (DNS), as the estimated number of grid points proportional to the 9/4 power of the Reynolds number which would require over 40 billion grid cells. Hence, the hybrid LBM-VLES approach is used for such low Mach number flows due to its numerical efficiency and computational benefits over Navier–Stokes based approaches (Krüger *et al.*, 2017; Moreau, 2019). Moreover, the present simulations being compressible, they can also yield the direct acoustic field as shown in Venkatraman *et al.* (2022).

The paper is organized as follows: the VAWT model used in the present study is described in Section 2, followed by the computational fluid dynamics model setup in Section 3. The results are discussed in Section 4, and the model predictions are compared with available experimental results. Finally, the conclusions and suggestions for future work are provided in Section 5.

2. VAWT experimental model
Weber *et al.* (2015) and Weber *et al.* (2016) studied the aerodynamics and aeroacoustics of a 1:5 scale H-Darrieus VAWT shown in Figure 1. The model of radius $R = 0.1$ m has three NACA0018 blades with a chord length of 0.05 m with an aspect ratio of 1. The geometrical parameters of the model are summarized in Table 1. The experiments were performed in an anechoic facility as shown in Figure 2 with a low turbulence intensity of 0.1%. The resulting

Figure 1.
Model VAWT rotor studied by Weber *et al.* (2015) and Weber *et al.* (2016)

Reynolds number based on the chord length and the tangential velocity ($R \times \omega$) ranging from 28,000 for a rotational speed ω of 800 rpm to about 211,000 for a rotational speed of 6,000 rpm. The kinematic viscosity of air at 18°C is taken to be 1.49×10^{-5} m^2/s. The thickness of the end plate is 1 mm. The rotor speed of the model was adjusted using the servomotor Siemens Simotics S1Fk7. The torque was measured using a torque sensor with a measuring range of 1 N m as shown in Figure 3. Once the power curve prediction has been validated, additional studies can also be performed to study the aeroacoustic characteristics of the turbine.
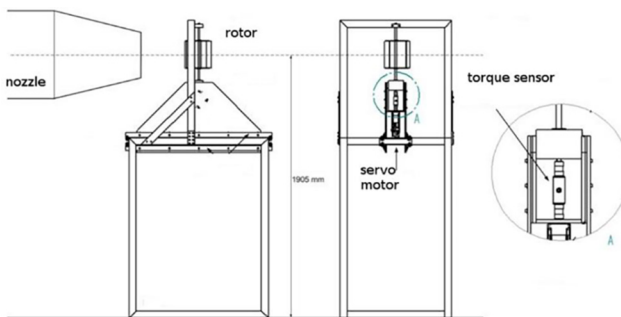
Parameter	Value
Profile	NACA 0018
Number of blades	3
Height	0.2 m
Diameter	0.2 m
Uniform freestream	21.28 m/s
Solidity	0.75
Reynolds number	28,000–211,000

Table 1.
Geometry
parameters

Source: Weber et al. (2015); Weber et al. (2016)

Figure 2.
Anechoic facility at
the Institute of
Process Machinery
and Technology
(IPAT), Erlangen

Source: Weber et al. (2015); Weber et al. (2016)

Figure 3.
Schematic diagram of
the torque
measurement setup
the Institute of
Process Machinery
and Technology
(IPAT), Erlangen

2.1 VAWT flow physics

The relative velocity experienced by a VAWT blade is the vector sum of the incoming wind velocity U_o and the velocity of the advancing blade $R \times \omega$ as shown in Figures 4 and is given by equation (1). Similarly, the geometric angle of attack α experienced by the blades is expressed by equation (2). Here, both are expressed in terms of the tip-speed ratio (TSR) ξ, defined as $(R \times \omega)/U_o$, and used as the parameter to define the different flow regimes for VAWTs:

$$W = |\mathbf{W}| = U_o \left[1 + \xi^2 - 2\xi\cos(\omega t)\right]^{1/2} \tag{1}$$

$$\tan(\alpha(t)) = \frac{\sin(\omega t)}{\xi - \cos(\omega t)} \tag{2}$$

2.1.1 Flow regimes for a VAWT. A typical power curve for a VAWT comprises of four different regimes: deep stall, dynamic stall, operational regime and parasitic drag regime (McIntosh *et al.*, 2009). For VAWTs with high solidity, the deep stall regime begins for a range of TSRs from 0.1 to 0.5. At low TSRs ($\xi < 1$) as seen from the velocity triangles, the blades experience angles of attack as high as 90° as shown in Figure 5, leading to a significant dynamic stall. Both the magnitude of the relative velocity and the angle of attack experienced by the blades vary over the azimuthal revolution of the blades. Due to the significant flow separation caused by the high angles of attack encountered by the blades almost negligible power is produced. The instabilities produced in this regime also impact the self-starting capability of the wind turbine (Dumitrescu *et al.*, 2015; Rainbird *et al.*, 2015). Increasing the TSR in the range 0.5–1.5 leads to the dynamic stall regime, where the power produced by a VAWT gradually increases, and the blades undergo a less severe dynamic stall due to a lower range of angles of attack experienced by the blades. The peak of the power coefficient is seen in the rated operational regime, for the present turbine, this is in the range of TSR from 1.5 to 2. Furthermore, with increasing TSR, the power produced by the wind turbine decreases resulting in a drop in the power coefficient which is defined as the parasitic drag regime.

2.1.2 Phases of a VAWT revolution. As per conventions utilized in Rezaeiha *et al.* (2017) and shown in Figure 6, the rotation of a Darrieus VAWT can be classified into four
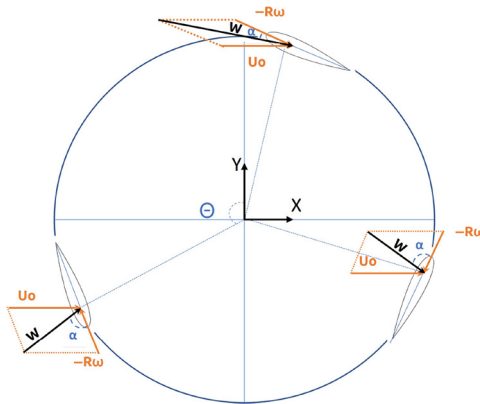
Figure 4.
Velocity triangle for a three-bladed Darrieus VAWT, with a uniform inflow coming from the left to the right
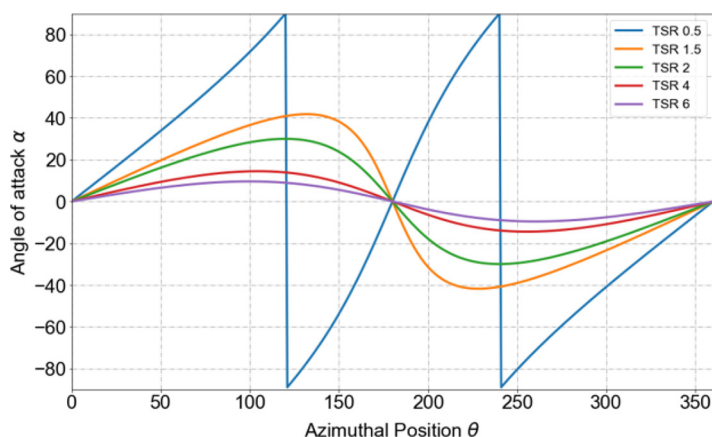
Figure 5.
Variation of the angle
of attack with the
azimuthal angle for
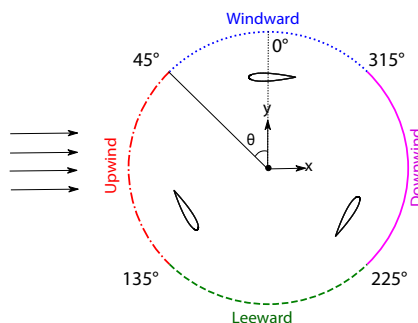different tip speed
ratios (TSR)

Source: Rezaeiha *et al*. (2017)

Figure 6.
Phases of a VAWT
rotation as per
conventions for a
counter-clockwise
rotation

different phases. The windward phase between ($315° < \theta < 45°$), the upwind phase between ($45° < \theta < 135°$), the leeward phase between ($135° < \theta < 225°$) and the downwind phase between ($225° < \theta < 315°$). The azimuthal angle θ is defined as the angle with respect to the positive y-axis.

3. Computational fluid dynamics model

3.1 Solution methodology

For the present study, an aeroacoustic simulation chain is achieved for VAWTs using the commercial lattice Boltzmann method (LBM) solver PowerFLOW version 6 from 3DS (Dassault-Systèmes, 2020). The experiment from Erlangen anechoic wind tunnel is simulated. The case setup offers the possibility to easily adapt and simulate different VAWT architectures such as the classical, helical or horizontal bladed rotors. It offers automated grid generation capability for the creation of an octree Cartesian grid and local refinement regions around the specified geometry. The flow solver has been validated for several benchmark cases across different industrial applications from energy to transport and heat and air-conditioning systems (Casalino *et al.*, 2021; Casalino *et al.*, 2018; Lallier-Daniels *et al.*, 2017; Moreau, 2019; Moreau and Sanjosé, 2016; Perot *et al.*, 2012; Romani and Casalino, 2019;

Sanjosé and Moreau, 2017; Zhu *et al.*, 2018). Note that all the validations achieved on low-speed fans correspond to a similar chord-based Reynolds number range as the present study. The LBM approach was chosen as it is inherently time-dependent, compressible and offers several computational advantages over Navier–Stokes methods in terms of ease of implementation, parallelization and speed (Krüger *et al.*, 2017; Moreau, 2019). It also offers low dispersive and dissipative properties (Moreau, 2022).

3.1.1 Lattice Boltzmann method methodology. The LB equation is given by equation (3). The LB method represents a mesoscopic definition of fluid particles. It solves the advection and collision of fluid particles with a specified velocity and finite direction using the particle distribution function represented as $F(x, t)$. The LBM is a finite difference solver of this equation implemented on a lattice (Chen and Doolen, 1998), for example, using 19 discrete velocity vectors in 3D space (D3Q19 lattice):

$$\frac{\partial F}{\partial t} + V \cdot \nabla F = C \tag{3}$$

where V is the particle velocity and C is the collision operator. The discretized form of the LB equation is shown in equation (4):

$$F_n(x + V_n \Delta t, t + \Delta t) - F_n(x, t) = C_n(x, t) \tag{4}$$

where F_n is the particle distribution function, V_n is the particle velocity in the nth direction. The collision term C_n follows the Bhatnagar–Gross–Krook model (Bhatnagar *et al.*, 1954) as shown in equation (5):

$$C_n = -\frac{\Delta t}{\tau} \left[F_n(x, t) - F_n^{eq}(x, t) \right] \tag{5}$$

where τ is the relaxation time, which depends on the temperature and fluid viscosity, and F_n^{eq} is the equilibrium distribution function.

After solving equation (4), the macroscopic flow variables such as density and velocity are derived by integrating the weighted distribution function as shown in equations (6) and (7):

$$\rho(x, t) = \sum_n F_n(x, t) \tag{6}$$

$$\rho u(x, t) = \sum_n V_n F_n(x, t) \tag{7}$$

The numerical flow solver uses the VLES approach to resolve the effects of the large scales of turbulence. A wall model adapted for the presence of mean pressure gradient effects is used to account for the larger dimensionless distance to the wall y^+. An effective turbulent relaxation time scale is calculated as given by equation (8) based on a variant of the RNG $k - \epsilon$ model (VLES approach) (Duda *et al.*, 2019):

$$\tau_{eff} = \tau + C_\mu \frac{k^2/\epsilon}{\sqrt{1 + \eta^2}} \tag{8}$$

with $C_\mu = 0.09$ and η is a parameter computed as a function of the local strain, vorticity and helicity. The modified relaxation time is used to calibrate the solver. Further details on the wall function implementation in PowerFLOW can be found in Anagnost *et al.* (1997), Duda *et al.* (2019); and Teruna *et al.* (2020).

3.1.2 Simulation domain. The flow domain is shown in Figure 7. Cylindrical zones are used to define different levels of grid refinement. The domain size is set to 50 D on all sides, where D is the diameter of the rotor to simulate the anechoic chamber where the experiments were carried out. Note that this is also beyond the computational domain size recommended in Balduzzi *et al.* (2016) and Rezaeiha *et al.* (2017).

The domain comprises an inner rotating zone and an outer stationary zone. The inner zone contains the wind turbine blades and the supporting structures forming the body fixed local reference frame. The exact VAWT geometry is immersed in an octree Cartesian grid made of cubic cells or voxels and the surface is facetized with surfels. The mesh has around 44 million voxels, and the surface mesh comprises 8 million surfels. The domain is meshed using ten variable refinement (VR) zones, with high mesh refinement close to the VAWT blades and supporting structures as seen in Figure 8, medium level of refinement in the region close to the rotating zone and low refinement further away. There is a 1:2 grid refinement or coarsening yielding the different VRs. The finest mesh size close to the blade is set to values to 0.5 mm, corresponding to about 100 points across the chord length of the blade. A close up of the variable refinement regions defined close the blades is shown in Figure 8.

At the outer stationary zone, a uniform fixed velocity (21.28 m/s) is imposed at the inlet and the ambient static pressure (101,325 Pa) at the outlet. The rotational speed is imposed for the rotor zone and is changed to obtain the different operating conditions. This is meant to reproduce the uniform flow coming out of the wind tunnel nozzle and the constant speed imposed by the electrical motor driving the wind turbine in the anechoic wind tunnel at the
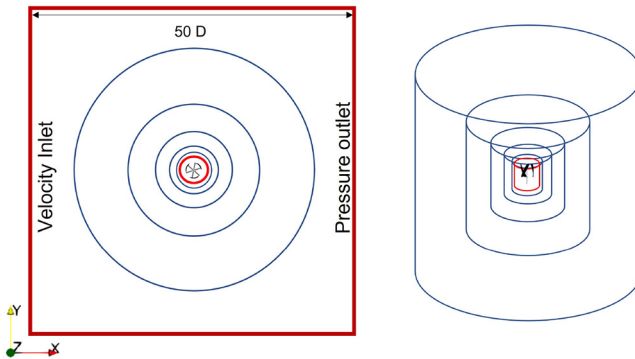

Figure 7.
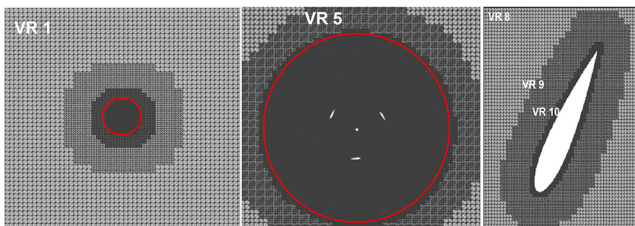Flow domain and cylindrical refinement regions

Figure 8.
Variable refinement regions shown for the entire simulation domain, zoomed close to the rotating zone and close to the rotor surface

Institute of Process Machinery and Technology, Erlangen (Weber *et al.*, 2015; Weber *et al.*, 2016). This is actually an ideal laboratory condition that will be different from the gusty, highly sheared flow encountered in urban environments. A sliding mesh interface is imposed between the rotating and stationary frames of the domain.

The simulation time step is fixed by the solver to 8.41E−07 s to obtain a CFL value of 1. Overall, the simulations are performed for at least 50 revolutions of the turbine to obtain converged statistics after neglecting the transient for the first 20 revolutions. Note that this is matching the minimum recommended simulation times in Lam and Peng (2016) and Rezaeiha *et al.* (2017), even though resolving the smallest turbulent scales even requires extra rotations compared to the uRANS cases.

3.2 Time and grid convergence study
A spatial mesh convergence study has been performed at a TSR of 1.23 (2,500 rpm) for three different values of smallest voxel sizes as shown in Table 2. This approach takes advantage of the octree grid setup, by suppressing the variable refinement regions close to the wall to generate a coarse grid. There is a less than 2% difference in the force magnitude between the three grids as seen in Table 2, although the variation is not monotonic with grid size. The variation of the tangential and normal force components on a single blade is shown for instance in Figure 9(a) and (b) for two revolutions of the wind turbine. The computed power coefficient C_p over 50 revolutions shows a negligible change in blade forces resulting in a variation of power coefficient C_p less than 10% between the three grids. The calculator methodology is provided in detail in Section 4.5. All simulations are further performed with the smallest voxel size set to 0.5 mm, resulting in a maximum dimensionless wall distance, y^+, of 40. For convergence in time, the coarse mesh (0.5 mm) has been simulated for around

Mesh	Minimum voxel size (mm)	Grid size (million voxels)	Simulation timestep (s)	Force (N)	C_p
Coarse	0.5	44	2.1E−07	3.85	0.19
Medium	0.25	60	4.21E−07	3.83	0.18
Fine	0.125	111	8.41E−07	3.90	0.20

Table 2.
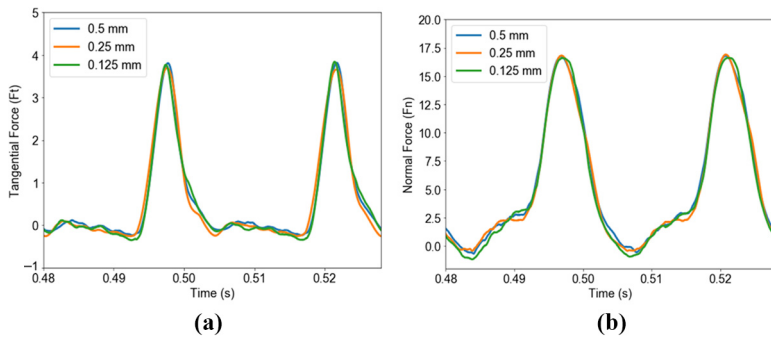Grid independence study

Figure 9.
Forces for a TSR of 1.23

Notes: (a) Tangential force variation on a single blade; (b) normal force variation on a single blade

120 revolutions, as shown in Figure 10. At least 20 revolutions are required to see a less than 0.2% change in the magnitude of the force on the blade similar to reported for some 2D uRANS studies (Rezaeiha *et al.*, 2017). Hence for all the calculations, the transient corresponding to the first 20 revolutions is discarded.

4. Results
The flow features of the model VAWT at three different operational points, corresponding to a tip-speed ratio of 0.4, 1.7 and 3 are analyzed below in terms of the instantaneous flow structures, mean velocity and pressure iso-contours, skin friction and blade loading. Finally, a comparison of the predicted power curve is made with the available experimental data.

4.1 Instantaneous flow structures
The instantaneous flow structures for a VAWT at different azimuthal positions are visualized using iso-surfaces of Q-criterion with a constant value of 13,000, and colored by velocity magnitude in Figures 11–13 for each operational flow regime. Complex turbulent flow structures of different scales are seen around the VAWT at all operating points. In the deep stall regime corresponding to a TSR of 0.4 (800 rpm) in Figure 11, the high angle of attack and flow separation results in large structures that formed close to the middle of the blade during the upwind phase seen for blade 1. The evolution of these dynamic stall structures and their subsequent interaction with the mast can be seen along the azimuthal rotation. This is similar to Posa and Balaras's observations in the same flow regime [blade B in Figure 15(a) and (b) in Posa and Balaras (2018)], but these large vortices do not form spanwise coherent rollers because of the end plates and their disruptive effect on the radial equilibrium along the blade. Tip vortices are also seen near the blade tip and the end plate junction but remain rather small because of the limited loading on the separated blade. These anisotropic flow structures further break up into smaller flow structures and interact with the mast and end plates on either side before impinging on the incoming blade in the downwind phase of rotation. As already noted by Posa and Balaras, the same blade 1 actually interacts with its own shed vortices [blade B in Figure 15(c) and (d) in Posa and Balaras (2018)]. In addition, flow separation and turbulent structures are seen for blade 2 in Figure 11(b) as the blade moves from the downwind phase to the windward phase. Thus, dynamic stall occurs both in the upwind phase and at the end of downwind phase. This results in an asymmetric wake, and the flow structures alternatively populate the windward and leeward sides. However, a difference is that in the upwind phase, the blade kinematics allows the development of large
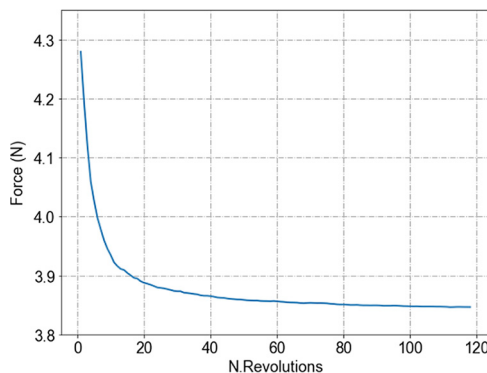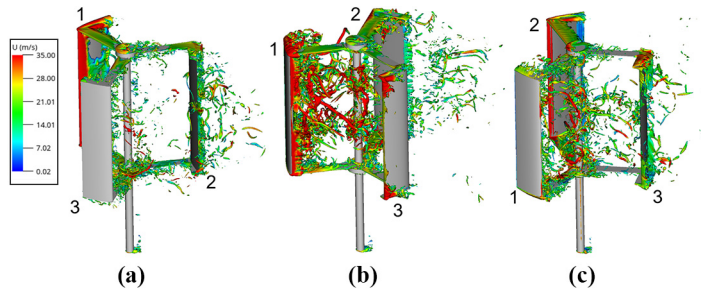

Figure 10.
Variation of force magnitude on a single blade with the number of revolutions for the coarse mesh (0.5 mm)

coherent flow structures, whereas in the downwind phase the shear layer separates and detaches quickly as the blade moves away from the flow structures.

In the operational regime corresponding to a TSR of 1.7 (3,500 rpm) shown in Figure 12, the main flow structures are the tip vortices and their interaction with the end plates, which
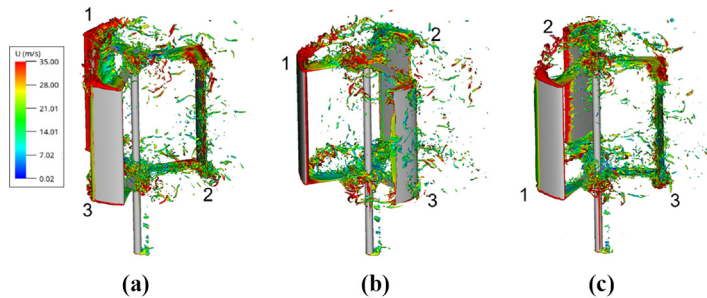
Figure 11.
Iso-contours of Q-criterion for TSR = 0.4 at different azimuthal positions

(a)   **(b)**   **(c)**

Notes: (a) 45°; (b) 90°; (c) 135° corresponding to blade 1 for an isovalue of 13,000

Figure 12.
Iso-contours of Q-criterion for TSR = 1.7 at different azimuthal positions

(a)   **(b)**   **(c)**

Notes: (a) 45°; (b) 90°; (c) 135° corresponding to blade 1 for an isovalue of 13,000

Figure 13.
Iso-contours of Q-criterion for TSR = 3 at different azimuthal positions

(a)   **(b)**   **(c)**
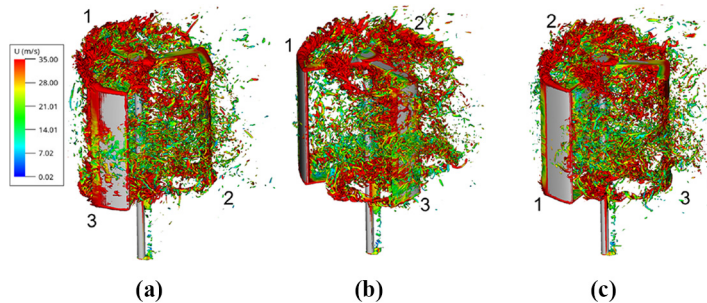
Notes: (a) 45°; (b) 90°; (c) 135° corresponding to blade 1 for an isovalue of 13,000

is significantly different from what Posa and Balaras observe in a similar flow regime [Figure 16 in Posa and Balaras (2018)]. In this regime, the blades encounter a lower range of angle of attack compared to the deep stall regime, resulting in lower flow separation and shed flow structures close to the mid-span of the blades. The resulting higher blade loading also triggers the larger and more intense tip vortices. Note also that at this peak efficiency condition, the main tip vortex interacts with the leading edge of the consequent blade. The azimuthal angle at which the flow structures are shed close to the trailing edge corresponds to the leeward phase of rotation as seen for blade 3 in Figure 12(b). This highlights the importance of including supporting structures and mast, as they modify the inflow experienced by the blades during the downwind phase and close to the tip. Additional scale-resolved simulations without the end plates and without both the end plates and the mast have been run to quantify these topological flow modifications and the associated losses by each structural element. Results are shown in the Appendix highlighting both changes in flow topology and additional power losses of 4 and 7%, respectively, when adding the mast alone, and the mast and the end plates.

Finally, for the parasitic drag regime shown for a TSR of 3 (6,000 rpm) in Figure 13, intense turbulence and small flow structures are seen to populate the inside part of the rotor. Here, the blade is moving at a high velocity, resulting in strong blade wake interactions and strong tip vortices. The size of the flow structures impinging on the blades in the downwind phase appears to be smaller in this flow regime, which highlights the importance of capturing flow structures inside the rotor accurately. In addition, both sides of the blades are impacted by these structures in the downwind half of rotation and there is double or even more impingement of the tip vortices from the two preceding blades and a large spreading of the wake that is dissipated quickly.

4.2 Phase averaged flow fields

To further quantify the different flow fields, the phase-locked averaged mean velocity contours at three different sections along the span corresponding to a z/H of 0.5, 0.75 and 1 are shown in Figures 14, 15 and 16, respectively. For each figure, the instantaneous velocity contours are averaged over five revolutions at the same azimuthal position. All figures are shown on the same scale between the different operating points. The flow separation from the leading and trailing edges of the blades and mean velocity deficit in the wake can be seen for a TSR of 0.4 (800 rpm) in Figure 14(a) at mid-span. The asymmetry in the wake and the trace of the tip vortices can also be seen in Figure 14(c). From mid-span to the side plates at the tip, there is a strong stratification of the flow with a wake mostly on the leeward side at mid-span, shifting to the windward side at the tip.

A stronger velocity deficit is seen inside the rotor for a TSR of 1.7 (3,500 rpm) shown in Figure 15 compared to the deep stall regime, with the wake forming the shape of a cone. A flow blockage region can also be seen in front of the rotor with the rotor beginning to behave as a rotating spinning cylinder, consistently with the transition of the wake of VAWTs to that of a bluff body reported experimentally by Araya *et al*. (2017) and numerically by Posa (2020b). Interestingly, a strong velocity deficit is seen toward the windward phase of rotation close to the end plates and near the tip in Figure 15(b) and (c) which is a similar vertical flow stratification that was seen in the deep stall regime. This deficit appears due to the vortices which are shed from the upwind phase of rotation which move toward the windward phase after interacting with the supporting structures as seen earlier in Figure 12.

At a TSR of 3 (6,000 rpm) shown in Figure 16, the wake shed by the wind turbine covers a larger cross-stream extent seen as a larger cone, as a result of the stronger tip vortices that are formed. Here, inside the rotor, the strength of the velocity deficit is lower, due to the flow

structures seen inside the rotor core, indicating that the blades perform poorly in extracting energy from the mean flow in the upwind phase. This is also consistent with a porous rotating cylinder spinning at a higher speed, with a large flow blockage region seen in front of the rotor, similar to the stagnation zone seen for a cylinder. An asymmetric wake is also seen in this regime, with the windward side showing a stronger deficit close to the tip as seen in Figure 16(b) and (c). The blades appear to reenter the wake with a high velocity.

The mean pressure iso-contours along the span corresponding to a z/H of 0.5, 0.75 and 1 are seen in Figures 17, 18 and 19, respectively. All figures are shown on the same scale between the different operating points. Higher pressure differences are seen as the rotational speed is increased, as expected as the blades experience higher loads. The interior of the rotor corresponds to a low-pressure zone with the inner side of the blades forming the suction side. The pressure in the center of the VAWT decreases and becomes more uniform with increasing TSR, consistent with the above velocity deficits (Figures 14–16) and the large separated flow and trapped flow structures seen in Figures 11–13. The highest loading where most of the energy extraction takes place appears to be in the upwind phase of rotation, as seen for blade 2. The strong trace of the tip vortices from blade 1 can be clearly seen as low-pressure regions for all flow regimes in Figures 17(c), 18(c) and 19(c).

Figure 14.
Phase-locked averaged mean velocity iso-contours for TSR = 0.4 at a span location of (a) z/H = 0.5, (b) z/H = 0.75 and (c) z/H = 1
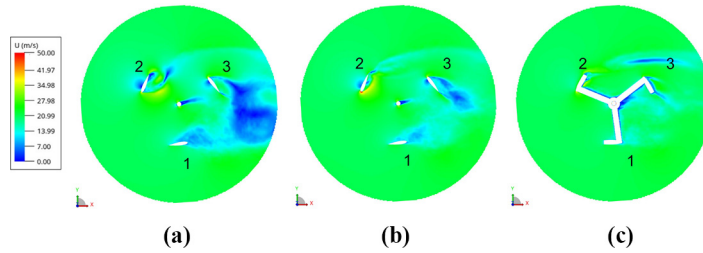
Figure 15.
Phase-locked averaged mean velocity iso-contours for TSR = 1.7 at a span location of (a) z/H = 0.5, (b) z/H = 0.75 and (c) z/H = 1
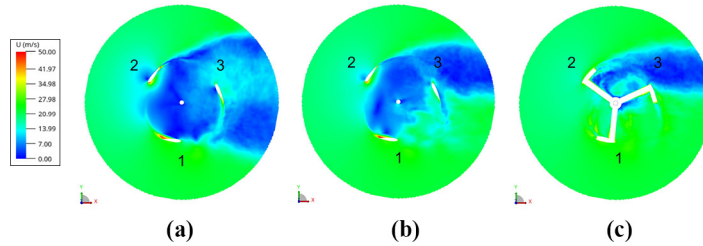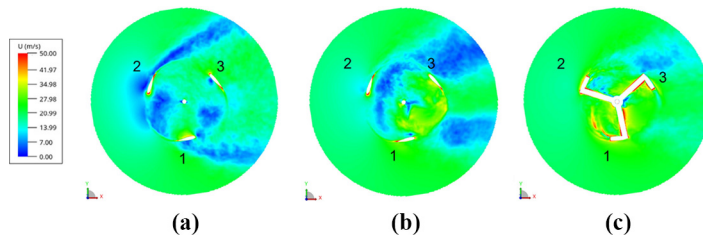
Figure 16.
Phase-locked averaged mean velocity iso-contours for TSR = 3.0 at a span location of (a) z/H = 0.5, (b) z/H = 0.75 and (c) z/H = 1

Overall, the wake shed from the VAWT across all regimes are seen to be asymmetric and a strong spanwise stratification is induced by the end plates. The higher the rotational speed, the higher the spreading of the cone-shaped wake. This is significant for VAWTs that could be placed in clusters to enhance their power density, indicating that there can be possibilities for optimal layout for these farms to minimize losses similar to horizontal axis wind turbines.

4.3 Skin friction contours

To better assess and quantify the flow separation on the VAWT blades, the skin friction contours along with surface streaklines across the blade span are shown in Figures 20–22 for each blade at a fixed azimuthal position for each operating point on the suction and pressure sides. In each figure, blade 1 corresponds to the leeward phase, blade 2 corresponds to the upwind phase and blade 3 corresponds to the windward phase. The scale of values for each figure is different and corresponds to the minimum and maximum values for each flow regime. A strong 3D flow with a clear disruptive effect of the end plates on the blade radial equilibrium is seen over the blades across a significant portion of the revolution, highlighting the necessity of 3D simulations for VAWTs on their actual 3D geometry including structural elements.
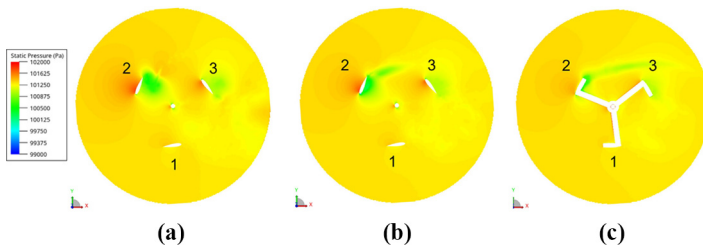

Figure 17.
Phase-locked averaged mean pressure iso-contours for TSR = 0.4 at a span location of (a) z/H = 0.5, (b) z/H = 0.75 and (c) z/H = 1
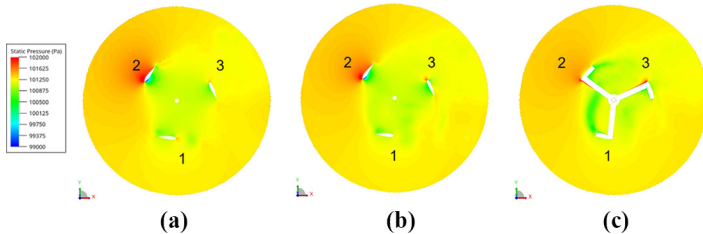

Figure 18.
Phase-locked averaged mean pressure iso-contours for TSR = 1.7 at a span location of (a) z/H = 0.5, (b) z/H = 0.75 and (c) z/H = 1
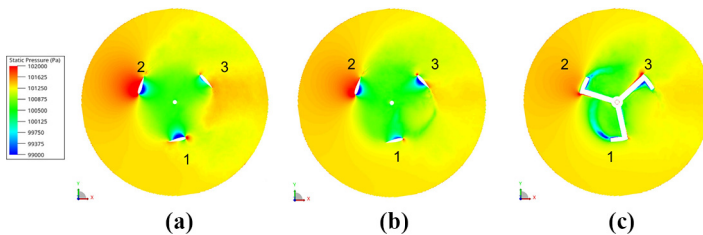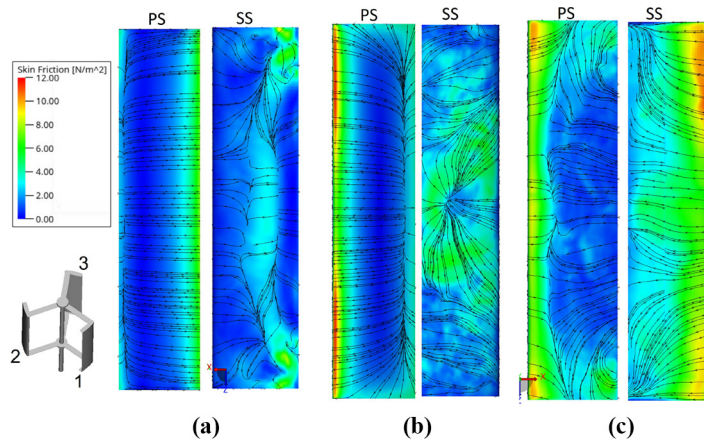

Figure 19.
Phase-locked averaged mean pressure iso-contours for TSR = 3.0 at a span location of (a) z/H = 0.5, (b) z/H = 0.75 and (c) z/H = 1

In the deep stall regime, a significant portion of blade 2 as seen in Figure 20(b) undergoes flow separation (zero skin friction) on both sides of the blades. The imprint of the dynamic stall structures is seen as shown earlier in Figure 11, where the leading edge vortex systems get convected across the blade surface before detaching completely. For blade 1 seen in Figure 20(a), on the suction side the imprint of the tip vortices and the vortex system close to the trailing edge (corner separation with saddle points as often found in shrouded turbomachines) can also be seen. Both the pressure and suction sides show evidence of flow separation as the blades again experience higher angles of attack while approaching the downwind phase of rotation. At blade 3 seen in Figure 20(c) the suction side appears to be mostly attached with the strong imprint of the tip vortices which affect almost 25% of the blade span on either side. On the pressure side, a significant part of the blade beyond the quarter chord shows flow separation shedding flow structures seen earlier in Figure 11(b).

Figure 21 shows the trace of the skin friction for the operational regime corresponding to a TSR of 1.7. As expected, higher skin friction is seen with increasing rotational speed at all positions. The flow appears to be more uniform across the span even though the disruptive effect of the end plates can still be seen (smaller corner vortices). The flow topology is also
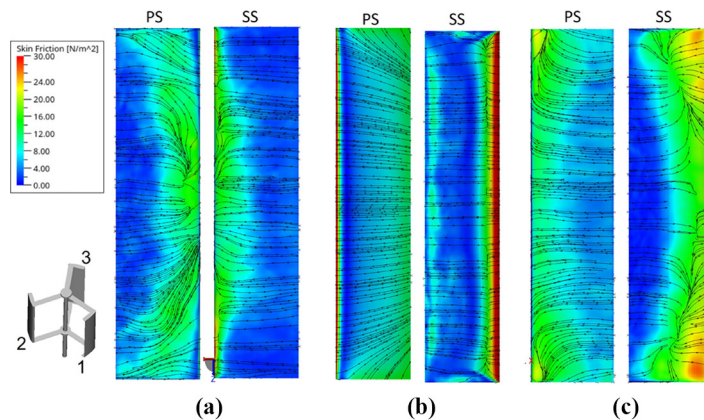
different compared to that seen in the deep stall regime. The suction side of blade 2 seen in Figure 21(b) shows the imprint of the trailing edge vortex system that develops in the upwind phase and finally sheds in the leeward phase of rotation. Significant flow separation is seen in Figure 21(a) for blade 1 on both the pressure and suction sides. The imprint of the tip vortices developed in the windward phase is visible on the suction side of blade 3 shown in Figure 21(c).

At a TSR of 3.0 shown in Figure 22, much higher skin friction and stronger imprint of the developed vortex systems across the leading edge, trailing edge and the tip is seen over all the blades. The most prominent separated region is seen when the vortex system detaches near the trailing edge at the end of the upwind phase for blade 2 on the suction side shown in Figure 22(b). For blade 1 seen in Figure 22(a), the impingement turbulent flow structures produced in the interior of the rotor (seen earlier in Figure 13) increase the skin friction on both the pressure and suction sides. Similar to the operational regime, a stronger imprint of the tip vortices induced by the end plates is seen for blade 3 in Figure 22(c) across a significant spanwise extent as the blade moves at high speed entering the wake of the previously shed turbulent flow structures. Finally note that the blade aspect ratio is not large enough to have a really 2D flow at midspan for any flow regime throughout a complete rotation, and even saddle points can locally appear as not reported before.

4.4 Force variation
The tangential forces induced on the blades are responsible for the production of torque and rotation of the wind turbine. The tangential forces for each blade F_{t_b} are computed by projecting the forces F_x and F_y extracted from the simulation in the global reference frame as illustrated in Figure 23. The net tangential force F_t for the rotor is computed by summing the contributions from each blade. Similarly, the normal forces are computed for each blade F_{n_b} by a coordinate rotation.

$$F_{n_b} = F_y cos(\theta) + F_x sin(\theta)$$
$$F_{t_b} = F_y sin(\theta) - F_x cos(\theta)$$
$$F_t = F_{t_{b1}} + F_{t_{b2}} + F_{t_{b3}}$$

The variation of tangential forces for a single revolution of the rotor is shown for different rotational speeds in Figures 24(a), 25(a) and 26(a).
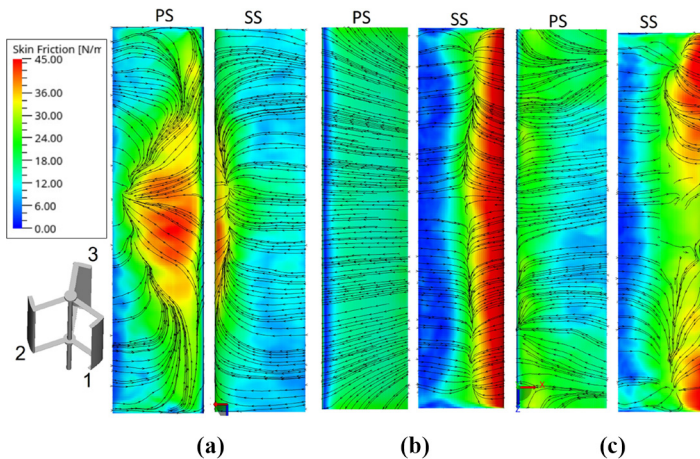

Figure 22.
Skin friction contours for TSR = 3.0 for (a) blade 1, (b) blade 2 and (c) blade 3 on the pressure side (PS) and suction side (SS)

At a low TSR of 0.4 seen in Figure 24(a), the tangential forces on the blade are very low in the range of 1 N, due to significant flow separation and dynamic stall as seen from instantaneous flow structures in Figure 11. The majority of the torque is produced during the upwind phase, and erratic fluctuations in the loading are seen in the downwind phase due to the flow structures shed in the upwind phase. The normal force components on the
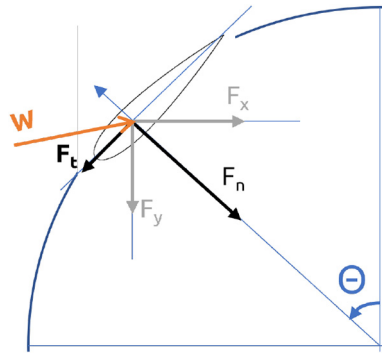
Figure 23.
Projection of the forces from the global reference frame to the local reference frame
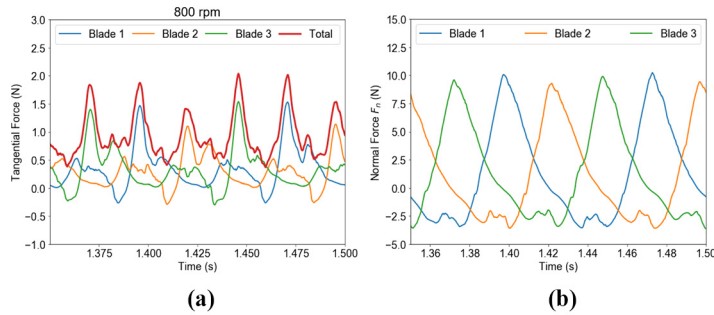

Figure 24.
Tangential and normal forces for TSR = 0.4

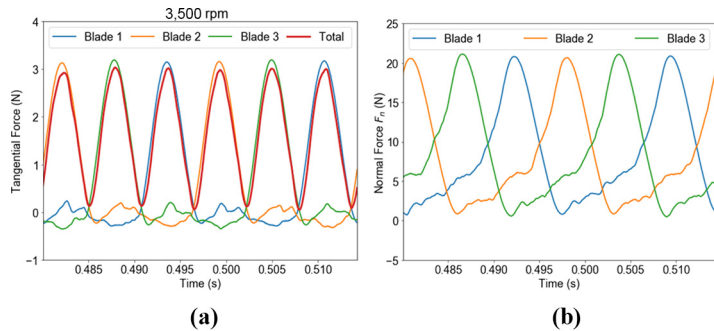**Notes:** (a) Tangential forces; (b) normal forces

Figure 25.
Tangential and normal forces for TSR = 1.7

Notes: (a) Tangential forces; (b) normal forces

blades are shown in Figure 24(b). A peak loading of about 10 N is achieved in the upwind phase of rotation with erratic fluctuations.

At the operational TSR of 1.7 seen in Figure 25(a), a smoother operation is seen for each blade in the upwind phase, where the majority of the torque is produced. Similarly to the deep stall regime, negligible torque is produced in the downwind phase with blade wake interactions. The peak tangential force produced by the system is in the range of 3 N. The normal force components on the blades are shown in Figure 25(b), which shows a peak blade loading in the order of 20 N and a less erratic variation compared to the deep stall regime.

Furthermore, in the parasitic drag regime seen for a TSR of 3 in Figure 26(a), the forces produced by the blades partially oppose each other, resulting in a lower net tangential force. In addition, strong and erratic fluctuations are seen due to the impulsive loading resulting from strong blade wake interactions in both the upwind and downwind phases. The erratic fluctuation of the normal force components on the blades is shown in Figure 26(b). Here, the blades experience very high loads, almost twice as much as experienced in the operational regime seen earlier.

At all three regimes, there is a cyclic variation of loads on the blades. Such a type of variation is inherent to the operation of Darrieus VAWTs and reduces their fatigue life. Moreover, in the case of urban VAWTs installed in urban environments, they need to be designed to withstand the peak loading could be experienced, and the structure upon which the wind turbine is installed must be capable of withstanding the peak loads and transmitted vibrations.

4.5 Power curve comparison

The torque T_z produced by the rotor is computed by multiplying the net tangential force F_t by the rotor radius. The power produced by the wind turbine is then computed as the product of the net torque and the corresponding rotational speed ω. The power coefficient C_p is calculated by normalizing the power P with the maximum available power P_{in} at the given wind velocity based on the rotor swept area A:

$$T_z = F_t \cdot R$$
$$P = T_z \cdot \omega$$
$$P_{in} = \frac{1}{2}\rho A W^3$$
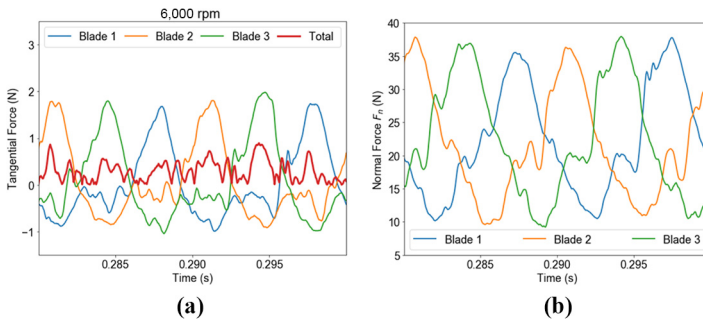$$A = D \cdot H$$
$$C_p = \frac{P}{P_{in}}$$

(a) (b)

Figure 26.
Tangential and
normal forces for
TSR = 3.0

Notes: (a) Tangential forces; (b) normal forces

A comparison of the experimental and predicted power curve is shown in Figure 27. The trend of the curve is captured by the model, with a close match at low tip-speed ratios. The power coefficient reaches a peak of 0.23. The peak value of the predicted power coefficient also shows a close match, about 2% higher than the experimental peak with an offset toward a higher TSR. However, the experimental uncertainties are not known and additional losses due to the measurement setup are not accounted for in the present calculations.

5. Conclusions

The aerodynamic performance of a complete model H-Darrieus VAWT with end plates and supporting structures was evaluated using the LBM-VLES approach. The predicted power curve provides a good overall match with the experimental power curve studied by Weber *et al.* (2015) at Erlangen University. The peak of the power curve and drop after the operational point is captured. At low TSRs, flow structures are shed in the upwind phase due to dynamic stall, developed as a consequence of the high angles of attack experienced by the blades. The end plates are seen to prevent the spanwise development of the shed large coherent structures and these vortices are further dislocated by impacting on the mast. The VAWT wake is then strongly asymmetric, with an additional stratification of the flow in the spanwise direction induced by the end plates. Almost negligible tangential force and power are produced in this regime. At the operational TSR, the flow structures are mainly concentrated close to the tip (a strong tip vortex caused by the higher loading and corner separations at the blade/end plate junctions), and they interact with the subsequent supporting end plates and blade. A smoother variation of the forces is seen on the blades over the revolution. The peak C_p value of 0.23 is reached in this regime. The wind turbine system begins to act like a porous spinning cylinder (transition to a bluff-body dynamics in the wake). The present study highlights the importance of considering the complete model setup and inclusion of support structures such as end plates and mast, which alters the flow developed across the rotor (disruptive effect on the blade radial equilibrium) and increases the losses produced by the turbine (7% at peak efficiency). At a higher TSR corresponding to the parasitic drag regime, intense turbulence is seen inside the rotor causing strong variations in forces on the blades. This results in a partial cancellation of forces between blades and increasing skin friction resulting in the drop in the power curve at high tip speed ratios. This highlights the importance of capturing flow structures inside the rotor accurately which is typically not possible with lower fidelity approaches such as uRANS

Figure 27.
Power curve comparison between the experimental (Weber *et al.*, 2015) and present numerical prediction
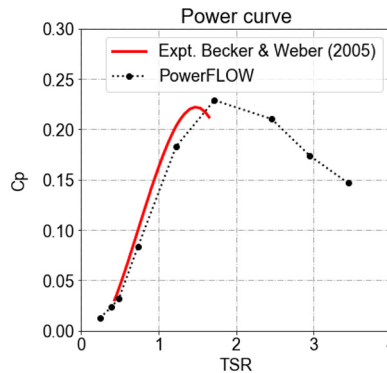
and other analytical models that are typically used in the literature. The 3D topology and complexity of the flow across the blade are illustrated using the skin friction plots, which highlights the importance of 3D simulations on the actual 3D geometry including the structural elements, especially for VAWTs with higher solidity and lower aspect ratio. At all flow regimes, the movement of the shed turbulent flow structures over the upwind phase revolution of the blades causes a strong near-wake asymmetry toward the windward phase of rotation. This needs further consideration for siting of arrays of VAWTs to increase their power density where the extent of the turbine wake, plays an important role in the overall performance of the VAWT cluster.

As future work, the impact of turbulent and nonuniform inflow conditions that are more representative of a typical urban environment needs to investigated. In addition, the possibility to improve existing analytical models such as Q-BLADE for VAWTs with high solidity needs to be evaluated. The angle of attack experienced by the blades can be calculated by sampling flow data at points close to the blade, to be fed as an input polar.

References

Amet, E., Maître, T., Pellone, C. and Achard, J.L. (2009), "2D numerical simulations of blade-vortex interaction in a Darrieus turbine", *Journal of Fluids Engineering*, Vol. 131 No. 11, pp. 1-15.

Anagnost, A., Alajbegovic, A., Chen, H., Hill, D., Teixeira, C. and Molvig, K. (1997), "Digital physics analysis of the morel body in ground proximity", *Journal of Passenger Cars: Part 1*, Vol. 106, pp. 306-312.

Araya, D.B., Colonius, T. and Dabiri, J.O. (2017), "Transition to bluff-body dynamics in the wake of vertical-axis wind turbines", *Journal of Fluid Mechanics*, Vol. 813, pp. 346-381.

Ardaneh, F., Abdolahifar, A. and Karimian, S. (2021), "Numerical analysis of the pitch angle effect on the performance improvement and flow characteristics of the 3-PB Darrieus vertical axis wind turbine", *Energy*, Vol. 239, p. 122339.

Balduzzi, F., Bianchini, A., Maleci, R., Ferrara, G. and Ferrari, L. (2016), "Critical issues in the CFD simulation of Darrieus wind turbines", *Renewable Energy*, Vol. 85, pp. 419-435.

Balduzzi, F., Zini, M., Molina, A., Bartoli, G., De Troyer, T., Runacres, M., Ferrara, G. and Bianchini, A. (2020), "Understanding the aerodynamic behavior and energy conversion capability of small Darrieus vertical axis wind turbines in turbulent flows", *Energies*, Vol. 13 No. 11, p. 2936.

Bhatnagar, P.L., Gross, E.P. and Krook, M. (1954), "A model for collision processes in gases. i. small amplitude processes in charged and neutral one-component systems", *Physical Review*, Vol. 94 No. 3, pp. 511-525.

Bianchini, A., Balduzzi, F., Ferrara, G. and Ferrari, L. (2016), "Dimensionless numbers for the assessment of mesh and timestep requirements in CFD simulations of Darrieus wind turbines", *Energy*, Vol. 97, pp. 246-261.

Biswas, A. and Gupta, R. (2014), "Unsteady aerodynamics of a twist bladed H-Darrieus rotor in low Reynolds number flow", *Journal of Renewable and Sustainable Energy*, Vol. 6 No. 3, p. 33108.

Casalino, D., Grande, E., Romani, G., Ragni, D. and Avallone, F. (2021), "Definition of a benchmark for low Reynolds number propeller aeroacoustics", *Aerospace Science and Technology*, Vol. 113, p. 106707.

Casalino, D., Hazir, A. and Mann, A. (2018), "Turbofan broadband noise prediction using the lattice Boltzmann method", *AIAA Journal*, Vol. 56 No. 2, pp. 609-628.

Chen, S. and Doolen, G. (1998), "Lattice Boltzmann method for fluid flows", *Annual Review of Fluid Mechanics*, Vol. 30 No. 1, pp. 329-364.

Dassault-Systèmes (2020), "Simulia powerflow user's guide".

Duda, B., Fares, E., Kotapati, R., Li, Y., Staroselsky, I., Zhang, R. and Chen, H. (2019), "Capturing laminar to turbulent transition within the LBM based CFD solver PowerFLOW", *AIAA Scitech Forum*.

Dumitrescu, H., Cardos, V. and Malael, I. (2015), *The Physics of Starting Process for Vertical Axis Wind Turbines*, Springer Tracts in Mechanical Engineering, pp. 69-81.

Elkhoury, M., Kiwata, T. and Aoun, E. (2015), "Experimental and numerical investigation of a three-dimensional vertical-axis wind turbine with variable-pitch", *Journal of Wind Engineering and Industrial Aerodynamics*, Vol. 139, pp. 111-123.

Franchina, N., Kouaissah, O., Persico, G. and Savini, M. (2019), "Three-dimensional CFD simulation and experimental assessment of the performance of a H-shape vertical-axis wind turbine at design and off-design conditions", *International Journal of Turbomachinery, Propulsion and Power*, Vol. 4 No. 3, p. 30.

Hannes, R. (2003), "HAWT versus VAWT: small VAWTs find a clear niche", *Refocus*, Vol. 4, pp. 44-46.

Karimian, S. and Abdolahifar, A. (2020), "Performance investigation of a new Darrieus vertical axis wind turbine", *Energy*, Vol. 191, p. 116551.

Krüger, T., Kusumaatmaja, H., Kuzmin, A., Shardt, O., Silva, G. and Viggen, E. (2017), *The Lattice Boltzmann Method, Principles and Practice*, volume 1 of Graduate Texts in Physics, Springer International Publishing, Switzerland.

Lallier-Daniels, D., Sanjosé, M., Moreau, S. and Piellard, M. (2017), "Aeroacoustic study of an axial engine cooling module using lattice-Boltzmann simulations and the Ffowcs Williams and Hawkings' analogy", *European Journal of Mechanics – B/Fluids*, Vol. 61, pp. 244-254.

Lam, H.F. and Peng, H.Y. (2016), "Study of wake characteristics of a vertical axis wind turbine by two and three-dimensional computational fluid dynamics simulations", *Renewable Energy*, Vol. 90, pp. 386-398.

Li, C., Zhu, S., Xu, Y. and Xiao, Y. (2013), "2.5D large eddy simulation of vertical axis wind turbine in consideration of high-angle of attack flow", *Renewable Energy*, Vol. 51, pp. 317-330.

McIntosh, S., Babinsky, H. and Bertényi, T. (2009), "Convergence failure and stall hysteresis in actuator disk momentum models applied to vertical axis wind turbines", *Journal of Solar Energy Engineering*, Vol. 131 No. 3, pp. 34502-34505.

Marten, D., Peukert, J., Pechlivanoglou, G., Nayeri, C. and Paschereit, C. (2013), "QBLADE: an open source tool for design and simulation of horizontal and vertical axis wind turbines", *International Journal of Emerging Technology and Advanced Engineering*, Vol. 3, pp. 264-269.

Moreau, S. (2019), "Direct noise computation of low-speed ring fans", *Acta Acustica United with Acustica*, Vol. 105 No. 1, pp. 30-42.

Moreau, S. (2022), "The third golden age of aeroacoustics", *Physics of Fluids*, Vol. 34 No. 3, pp. 1-15.

Moreau, S. and Sanjosé, M. (2016), "Sub-harmonic broadband humps and tip noise in low-speed ring fans", *The Journal of the Acoustical Society of America*, Vol. 139 No. 1, pp. 118-127.

Perot, F., Kim, M. and Meskine, M. (2012), "NREL wind turbine aerodynamics validation and noise predictions using a lattice Boltzmann method", *AIAA/CEAS Aeroacoustics Conference, number AIAA 2012-2290 paper in 2012-2290*.

Posa, A. (2020a), "Dependence of the wake recovery downstream of a vertical axis wind turbine on its dynamic solidity", *Journal of Wind Engineering and Industrial Aerodynamics*, Vol. 202, pp. 1-12.

Posa, A. (2020b), "Influence of tip speed ratio on wake features of a vertical axis wind turbine", *Journal of Wind Engineering and Industrial Aerodynamics*, Vol. 197, pp. 1-12.

Posa, A. and Balaras, E. (2018), "Large eddy simulation of an isolated vertical axis wind turbine", *Journal of Wind Engineering and Industrial Aerodynamics*, Vol. 172, pp. 139-151.

Qin, N., Howell, R., Hamada, K., Durrani, N. and Smith, T. (2008), "Unsteady flow simulation and dynamic stall around vertical axis wind turbine blades", *Journal of Wind Engineering*, Vol. 35 No. 4, pp. 510-511.

Rainbird, J., Ferrer, E., Peiro, J. and Graham, M. (2015), *Vertical-Axis Wind Turbine Start-Up Modelled with a High-Order Numerical Solver*, Springer Tracts in Mechanical Engineering, pp. 37-48.

Rezaeiha, A., Kalkman, I. and Blocken, B. (2017), "CFD simulation of a vertical axis wind turbine operating at a moderate tip speed ratio: guidelines for minimum domain size and azimuthal increment", *Renewable Energy*, Vol. 107, pp. 373-385.

Romani, G. and Casalino, D. (2019), "Rotorcraft blade-vortex interaction noise prediction using the lattice-Boltzmann method", *Aerospace Science and Technology*, Vol. 88, pp. 147-157.

Sanjosé, M. and Moreau, S. (2017), "Direct noise prediction and control of an installed large low-speed radial fan", *European Journal of Mechanics – B/Fluids*, Vol. 61, pp. 235-243.

Teruna, C., Manegar, F., Avallone, F., Ragni, D., Casalino, D. and Carolus, T. (2020), "Noise reduction mechanisms of an open-cell metal-foam trailing edge", *Journal of Fluid Mechanics*, Vol. 898, p. 2020.

Venkatraman, K., Moreau, S., Christophe, J. and Schram, C. (2021), "Numerical investigation of the effect of inflow non-uniformity on the noise radiated by a vertical axis wind turbine", *AIAA Aviation Forum*.

Venkatraman, K., Moreau, S., Christophe, J. and Schram, C. (2022), "H-Darrieus vertical axis wind turbine power prediction using the lattice Boltzmann approach", *56th 3AF International Conference on Applied Aerodynamics*.

Weber, J., Becker, S., Scheit, C., Grabinger, J. and Kaltenbacher, M. (2015), "Aeroacoustics of Darrieus wind turbine", *International Journal of Aeroacoustics*, Vol. 14 Nos 5/6, pp. 883-902.

Weber, J., Riedel, S., Prass, J., Renz, A., Becker, S. and Franke, J. (2016), "Effect of boundary layer tripping on the aeroacoustics of small vertical axis wind turbines", *Advanced Engineering Forum*, Vol. 19, pp. 3-9.

Wu, Z., Wang, Q., Bangga, G. and Huang, H. (2020), "Responses of vertical axis wind turbines to gusty winds", *Proceedings of the Institution of Mechanical Engineers, Part A: Journal of Power and Energy*, Vol. 235 No. 1, pp. 81-93.

Zamre, P. and Lutz, T. (2022), "Computational fluid dynamics analysis of a Darrieus vertical axis wind turbine installation on the rooftop of buildings under turbulent inflow conditions", *Wind Energy Science*, Vol. 7 No. 4, pp. 1661-1677.

Zhu, T., Lallier-Daniels, D., Sanjosé, M., Moreau, S. and Carolus, T. (2018), "Rotating coherent flow structures as a source for narrow band tip clearance noise from axial fans", *Journal of Sound and Vibration*, Vol. 417, pp. 198-215.

Appendix. Effect of end plates

The influence of end plates has been studied at the operational speed of 3,500 rpm. The power coefficient decreases by about 7% with the addition of end plates and mast, which results in increased losses at the tip. A 4% difference is already caused by the mast alone as summarized in Table A1. The mast has a slightly more important effect compared to the end plates which are only 1 mm thick for the present case. A visualization of the iso-surfaces of instantaneous flow structures for both cases is shown in Figure A1. Including the end plates and mast helps in a quicker breakdown of flow structures in the interior of the rotor. The presence of the end plates also seem to strengthen the tip vortex shed from blade 1 that separates earlier from the blade tip and has a bigger diameter [Figure A1(a)].

Table A1.
Power coefficient for the different cases investigating the effect of including end plates and mast

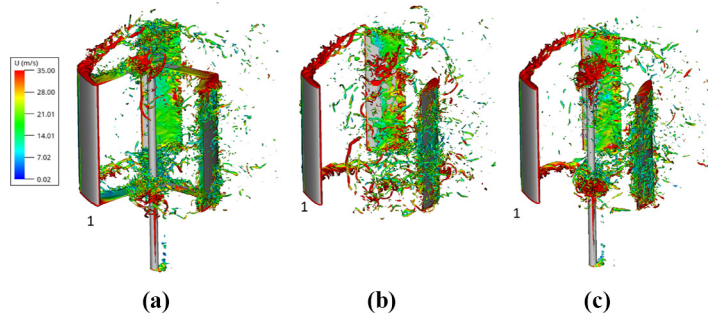| Case	C_p
With end plates and mast	0.228
Without end plates	0.237
Without end plates and mast	0.244

Figure A1.
Instantaneous flow structures visualized using iso-surfaces of Q-criterion with a value of 13,000 for case

Notes: (a) With end plates and mast; (b) without end plates and mast; (c) without end plates corresponding to an azimuthal position of 135° for blade 1

Corresponding author
Kartik Venkatraman can be contacted at: kartik.venkatraman@usherbrooke.ca